national accelerator laboratory

TM-358
2610.900

MUON IDENTIFICATION USING MULTIWIRE PROPORTIONAL CHAMBERS*

F.A. Harris, S.I. Parker, V.Z. Peterson and D.E. Yount
Department of Physics and Astronomy
University of Hawaii
Honolulu, Hawaii 96822 U.S.A.

M.L. Stevenson
Lawrence Berkeley Laboratory
University of California
Berkeley, California 94720 U.S.A.

*Work supported in part by the U. S. Atomic Energy Commission and the National Science Foundation.

ABSTRACT

Test data are summarized for a muon identifier consisting of iron absorber plates followed by multiwire proportional chambers. Because of the penetrating secondaries that result from hadronic interactions, conventional muon identifiers lacking spatial resolution require many collision lengths to attenuate, and thus to separate incident hadrons from muons. By using multiwire proportional chambers, hadronic interactions can be detected well before the subsequent hadron cascades have been fully absorbed. This permits a substantial reduction in absorber thickness and is important in applications in which the muons originate in a large volume or in which they are to be identified over a large area or large solid angle. A typical result from these tests is that at 3 GeV/c a single multiwire proportional chamber, following only 50 cm of iron, can reject pions with 96 ± 1% efficiency while accepting 96% of the incident muons. An important advantage of this technique is that the performance is expected to be rather independent of energy above a few GeV.

I. INTRODUCTION

The importance of muon identification in experiments involving high-energy incident neutrinos has frequently been emphasized.[1] Most neutrino interactions cannot be fully analyzed without muon identification, and it is explicitly required in some of the most promising areas of investigation: deeply-inelastic scattering, searches both for heavy leptons and for certain decay modes of intermediate-vector-bosons, studies of four-Fermion interactions, and the analysis of rare or unexpected events. This paper gives test data for a specific technique of identifying muons that appears to be well suited to studying neutrino interactions in a large bubble chamber.

In a classic muon range detector, such as that used in the SLAC 20-GeV spectrometer,[2] muons are distinguished from hadrons purely on the basis of penetrating radiation. An absorber having a thickness of 15 collision lengths (about 200 cm of iron) is sufficient to contain the penetrating secondaries in a hadron cascade, and a simple null signal deep in the absorber then suffices to classify the incident particle as a hadron. This technique, based essentially on range alone, is particularly successful in the case of the 20-GeV spectrometer because any charged particles reaching the range detector are moving nearly parallel with virtually the same momenta.

The problem of identifying muons from neutrino interactions in a large bubble chamber is a great deal more

difficult than that faced by the SLAC 20-GeV spectrometer. Not only is the muon source now a large volume, but further, the muons emerge with a wide range of angles and momenta. To intercept a useful fraction of these muons, the identifier must cover a large area ($\sim$ 50 m^2 for NAL) and a large solid angle ($\sim \pi$ ster), and it must be able to distinguish muons in a sea of hadrons in which the energies vary by two orders of magnitude and in which some of the hadrons may even originate in the same interaction as the muon being examined.

A thick absorber is required in the classic muon-range detector largely because the occurrence of an hadronic interaction is not apparent until all of the charged secondaries have been absorbed. This limitation can be overcome by using detectors with sufficient spatial resolution to distinguish the large-angle scatters and multi-prong topologies associated with hadronic interactions. The bubble chamber itself is an excellent example of such a high-resolution detector, and muons could readily be identified by their failure to interact strongly in the bubble chamber liquid, providing a sufficient path length were available.

In the technique under investigation here, charged particles emerging from an absorber are detected by a single plane of multiwire proportional chambers that provides x, y, and diagonal coordinates for each emerging track. It is assumed that both the presence and the trajectory of each incident track are known from an analysis of the bubble chamber

film. By taking into account multiple scattering in the absorber, as well as the uncertainties in the incident trajectory, a region can be defined in the detector plane in which the incident particle, if it is a muon, is likely to appear. Hadrons, on the other hand, normally interact strongly in the absorber, sending any reaction products outside the muon-acceptance region. The possibility of using a second absorber and detector plane is also very promising, but of course the cost and complexity of the identifier are correspondingly greater.

In the classic muon-range detector, the reaction secondaries tend to penetrate deeper into the absorber as the incident energy increases. This is evident in Fig. 1, where we have plotted pion-range data obtained with the SLAC 20-GeV spectrometer.[2] In this figure, the ordinate gives the fraction of the pions surviving versus the equivalent thickness of iron absorber in cm for negative incident momentum settings of 4.7, 7.7, 10.7, and 15.8 GeV/c. Muon identifiers that depend solely on attenuating the penetrating radiation are thus energy-dependent and require increasing absorber thicknesses as the energy goes up. This would be a serious disadvantage in applications, such as our own, in which particles with a wide range of momenta are incident simultaneously. Fortunately, the nuclear reaction cross section itself is relatively constant, which accounts for the fact that the curves in Fig. 1 for different momenta ultimately have similar slopes.

The slopes correspond approximately to an attenuation length of 21 cm of iron, where the expected collision length for iron is 12.8 cm.[3] It also implies that the present technique, based on early detection of individual hadronic interactions, should be relatively insensitive to energy.

Multiwire proportional chambers are ideal detectors in this application since they require no trigger, are continuously sensitive, work well in high magnetic fields, and can be operated with negligible deadtime. The spatial resolution used in these tests is rather better than is actually required in the bubble chamber application, and this should permit a substantial reduction in the cost and complexity of the final chambers, readouts, and data-handling systems.

The experimental apparatus used in these tests is described in Section II, and the methods of data analysis and calibration are discussed in Sections III and IV. The actual experimental results for incident muons and pions are summarized, respectively, in Sections V and VI.

II. EXPERIMENTAL APPARATUS

In order to determine the pion-rejection efficiency (or the muon acceptance) of our proposed muon identifier, it is necessary first to establish a pion (or muon) beam. The experimental apparatus, which distinguishes pions and muons and also simulates the muon identifier, is shown schematically in Fig. 2a. The muon identifier is represented by two iron absorbers, A1 and A2, of variable thickness; a variable drift space d; and the x-y proportional-chamber pairs, PC1 and PC2. Momentum-analyzed particles from the Bevatron are incident from the left, and a narrow beam is defined by the 1.3 cm x 1.3 cm scintillation counters S1 (not shown) and S2, which are separated by 200 cm. The distance between S2 and PC1 is 130 cm. A high-pressure gas Cerenkov counter (not shown) is located 20 m upstream of S1 and allows us to distinguish π's and μ's from protons by velocity selection when the beam is positive. (The tests reported here are from a parasitic run with the beam often positive.) The counters S4 and S5, 30 cm x 30 cm and 45 cm x 55 cm, respectively, and additional iron absorbers, A3 to A6, allow separation of π's and μ's by the conventional method of absorbing out the pions. The 20 cm x 20 cm counter S3, which is immediately behind PC2, is not normally included in the particle trigger but is used to measure the efficiency of PC1 and PC2 when the iron blocks A1 and A2 are removed.

Beam studies are conducted by varying the locations of

the counters S4 and S5 in the absorber. Figure 3 shows the attenuation of a positively-charged, 3 GeV/c beam as a function of the total amount of iron in front of S5. The upper curve ($\frac{S1\ S2\ S4\ S5}{S1\ S2}$) contains protons, pions, and muons, but the lower curve has the Cerenkov counter in coincidence and therefore contains primarily pions and muons. For a positively-charged beam, μ's are defined by S1 S2 S4 S5 C, and π's are defined by S1 S2 $\overline{S5}$ C. For the muon-identification tests at 3 GeV/c, the location of S5 corresponds typically to 150 cm of Fe, which is well out on the muon plateau. The placement of S5 in the iron absorber is chosen so that the pion contamination in the μ trigger is less than 3% while less than 6% of the muons are lost because of multiple Coulomb scattering. Pions and muons amounted to 7.5% and 0.3% of the positive-particle flux, respectively.

Accidentals in the pion trigger are determined by delaying the pulse from the high-pressure Cerenkov counter by 400 nsec, which corresponds approximately to the Bevatron RF period. The accidental rate varies between 2% and 5% of the pion rate, depending on the beam intensity. These events are interpreted as real pions counting in the high-pressure counter in time-coincidence with protons counting in S1 and S2. The electron contamination was measured to be 0.1% and was negligible compared with the proton contamination.

Another form of background in the pion beam is due to muons which are not vetoed by S5. S5 does not detect muons

with a momentum less than 2 GeV/c, corresponding to a range in iron of less than 150 cm. Such μ's arise from π-μ decay after the last bending magnet. The contribution of these events is calculated by dividing the 8-m decay region after the last magnet into small segments. For each segment the fraction of the decay muons intercepted by S2 is determined and then multiplied by both the number of incident pions and the pion-decay probability per segment. The total number of decay muons is found by summing the contributions of each of the segments. Except for a short region just in front of S2, the counter selects forward muons of high ($P > 2.9$ GeV/c) and low ($P < 1.8$ GeV/c) momentum. The low-energy muon contamination with $P < 2$ GeV/c is estimated to be 0.4%. In addition, some high-energy μ's could multiple Coulomb scatter and miss S5. The contribution due to this effect is estimated to be 0.2%.

Accidentals in the muon trigger are also determined by delaying the pulse from the high-pressure Cerenkov counter and are found to be less than 1% of the muon rate. The combined Cerenkov and range requirement yields a muon trigger with relatively little background, even though muons comprise a small fraction of the particle flux, but the pion decays after the last bending magnet provide muons with a large spread in momentum. From the above calculation, it is found that over 90% of muons detected by S5 were in the momentum range from 2.9 to 3 GeV/c. The number of pions remaining after 150 cm of iron is estimated to be less than 3% from the range curve.

The construction of the proportional chambers is discussed in detail elsewhere.[4] The wires of the sensitive-plane are 20 μm in diameter, spaced 2 mm apart, and they form a plane with sensitive area 19 cm x 20 cm. Only the sensitive plane is read out, yielding one coordinate per chamber, so that two chambers and associated readout electronics are necessary at each of the locations PC1 and PC2 to provide x and y coordinates. The chambers and electronics are contained in a copper RF shielding box made from 30-mil copper sheeting, and the temperature in the boxes is stabilized to provide reliable operation of the readout electronics.

The sensitive-plane wires are tied together in pairs and are read out into 48 amplifier-discriminator channels. Discriminator thresholds are adjusted with a 6-KeV ^{55}Fe source, so that x-rays corresponding to an ionization of approximately 0.6 KeV would be above threshold. Pions traversing the chamber have a most probable energy loss of 3.5 KeV. When a single particle is detected, the readout electronics supplies a 3.5 μsec logic-level pulse, the 'event' pulse, and a digital pulse train corresponding to the channel number of the wire that triggered. The same 3.5 μsec pulse gates off the readout internally and is also used externally to gate off the scintillation counters, S1 → S5, thus providing an effective readout deadtime. The event pulse is also scaled and can be used to determine chamber efficiencies, using S3 as a monitor.

A digital-to-analogue converter allows the channel-number

information to be displayed on an oscilloscope, and the x-y coordinates at PC1 and PC2 are simultaneously displayed on a Tektronix 556 dual-beam oscilloscope by intensifying the beam spots with a pulse from the fast electronics for particles satisfying the π or μ trigger. Data are recorded either with a Polaroid camera (many events per picture) or with a 35-mm Flight Research camera (individual events). Polaroid data are used to study the pion rejection by a one-plane detector (for two absorber thicknesses at once), and the 35-mm data allow a study of the pion rejection of a two-plane detector, since correlations of particle positions at PC1 and PC2 could be determined. S3 is also required in the pion trigger for the 35-mm data, since otherwise most of the film would be blank.

If more than one particle is detected at a proportional-chamber wire plane during a resolution time of 75 nsec, the electronics produces a "multiparticle-event" pulse, another logic level pulse, but does not supply any coordinate information. The multiparticle-event pulses corresponding to the x and y planes are combined passively, and coincidences with the π or μ trigger are scaled separately for PC1 and PC2. In this way, the number of multiparticle events is determined even though multiparticle coordinate information is beyond the scope of the electronics. The readout electronics then distinguishes three types of events: 1) no charged particle detected, 2) one charged particle detected, and 3) more than one charged particle detected.

III. DATA ANALYSIS AND CALIBRATION

The x-y coordinate locations on the film are measured on a digitizing machine, and the information is recorded on computer cards for ease of data handling. Examples of x-y displays composed of many events superimposed on a single Polaroid photo are shown in Fig. 4. Particles with valid x and y coordinates are spread out over the area of the chamber, and particles detected in either x or y only occur at the extreme left or extreme bottom of the chamber display. These points may occur because: 1) one chamber is inefficient, 2) one chamber detects a multiparticle event when the other detects only a single track, or 3) the particle is outside the sensitive region of one of the chambers. Triggers for which both chamber planes detect either a multiparticle event or no particle occur at the lower-left corner of the chamber display.

Figure 4a shows the results of a 3 GeV/c π^- run with A1 = 30 cm, A2 = 30 cm, and d = 94 cm (see Fig. 2a). In this particular run, there are 1453 incident π^- for which PC1 indicates 235 events and PC2 indicates 56 events, all of these PC1 and PC2 events having a valid x and y. In addition, there are 32 multiparticle events and 39 events detected in only x or y in PC1; and there are 15 multiparticle events and 28 events detected in only x or y in PC2. Evidently, the majority of the incident pions are not detected by the multiwire chambers, and most of them are either completely absorbed or

are scattered outside the area of the detector.

In determining the efficiency of the chambers we do not use the number of points detected in only x or y, since this is some unknown combination of the three possibilities listed above. Instead, we measure directly the efficiency over a portion of the chamber and compare this result with the instrumental efficiency for detecting muons, which is discussed in Section V. The direct efficiency measurement is made with the absorbers A1 and A2 removed, using S1 S2 S3 as the monitor. The efficiency is the sum of the event pulses, plus the multiparticle event pulses, divided by the monitor. We find that PC1 has a typical overall efficiency (detection by both planes) of 97%, while the efficiency of PC2 is typically 95%. These efficiencies are measured over a fairly small region of the chamber, which corresponds to the size of the beam spot with no absorber. An example of the scope displays obtained with no absorber is shown in Fig. 4b.

We can use the efficiency to correct the number of points detected by both the x and the y planes and thus obtain two important numbers, which we will use in the analysis: 1) the corrected number of particles detected by the chamber and 2) the number of multiparticle events. We could estimate the pion rejection by assuming that the muon detector corresponds to the entire chamber (events not detected by the chamber are identified hadrons), but we can go even further. Single events within the PC1 and PC2 displays can also be identified

as hadrons if they occur outside of the region in which incident muons would lie. The definition of this region depends to some extent on how well the incident beam direction and position are known, but in these tests the main limitation is multiple Coulomb scattering. Essentially, we are interested in the number of hadrons remaining in a circle that would contain a given fraction, say 96%, of the incident muons. Particles outside the circle can then be considered as identified hadrons.

IV. MULTIPLE COULOMB SCATTERING

The effect of multiple Coulomb scattering on the spatial distribution of an infinitesimally narrow, parallel beam passing through an array of absorbers and drift spaces may be calculated by a simple technique.[5] This technique may be interpreted in the following manner. Assuming that we can use the Gaussian approximation to the multiple-scattering distribution,[6] the mean-squared radius of the distribution, after passing through an absorber of thickness t_o and a drift space of distance d_o is given by

$$\overline{R_o^2} = \overline{\theta_o^2} \left(\frac{t_o^2}{3} + t_o d_o + d_o^2\right) .$$

$\overline{\theta_o^2}$ is the mean-squared scattering angle due to the absorber and is given by

$$\overline{\theta_o^2} = \left[\frac{21(\text{MeV})}{PV(\text{MeV})}\right]^2 \left(\frac{t_o}{t_{rad}}\right) ,$$

where P and V are the momentum and velocity of the particle and t_{rad} is the radiation length of the absorber. If a second absorber with thickness t_1, drift space d_1, and scattering angle θ_1 is placed inside the drift space of the first absorber, then the total contribution to the mean-squared radius will be

$$\overline{R^2} = \overline{R_o^2} + \overline{R_1^2} ,$$

where

$$\overline{R_1^2} = \overline{\theta_1^2}\left(\frac{t_1^2}{3} + t_1 d_1 + d_1^2\right) ,$$

since the contribution of the second absorber to the spatial distribution is independent of the first absorber for small displacements. For an array of n absorbers, then, the total contribution at the back of the array is given by

$$\overline{R^2} = \sum_{i=1}^{n} \overline{R_i^2} ,$$

where the $\overline{R_i^2}$ depend only on the angle of scattering in absorber i, the thickness of absorber i, and the distance from the back of absorber i to the end of the array. This technique for analyzing a series of absorbers and drift spaces also allows one to subdivide a thick absorber into small sections in order, for example, to include energy loss in the absorber.

The rms radius for multiple scattering as a function of distance at 3 GeV/c for a typical geometry (A1 = 30 cm, A2 = 30 cm, d = 94 cm) is shown in Fig. 2b. The rms radius at PC2 for this configuration is, for example, 6 cm.

The distribution of particles in terms of the rms radius may be obtained from the one-dimensional distributions

$$N(x) = \frac{1}{\sqrt{2\pi\sigma^2}} e^{-x^2/2\sigma^2} ,$$

where $\sigma = x_{rms} = y_{rms} = R_{rms}/\sqrt{2}$. In two dimensions, this becomes

$$N(x)\ N(y) = \frac{1}{2\pi\sigma^2}\, e^{-x^2/2\sigma^2}\ e^{-y^2/2\sigma^2} = \frac{1}{\pi R_{rms}^2}\, e^{-r^2/R_{rms}^2}\ .$$

The fraction of the particles contained in a circle of radius r_o is then given by

$$N(r_o) = \frac{1}{\pi R_{rms}^2} \int_o^{2\pi} \int_o^{r_o} e^{-r^2/R_{rms}^2}\ r dr d\theta = 1-e^{-(r_o/R_{rms})^2}\ .$$

The radius of a circle containing 96% of the muons is $R_{96\%} = 1.78\ R_{rms}$. For some of our configurations, PC2 is geometrically smaller than $R_{96\%}$, so that only part of our data is useful in calculating the pion-rejection efficiency in PC2.

The non-zero width and the divergence of the beam are taken into account by combining in quadrature the size of the beam spot at PC1 and PC2 using no absorber with the calculated root-mean-square radius for multiple Coulomb scattering. The beam spot is approximately circular at the locations of PC1 and PC2, and the effective radii are 1.3 cm and 1.5 cm, respectively (see Fig. 4b). For most runs, the beam-spot size is considerably smaller than the contribution due to multiple Coulomb scattering, so that uncertainties in the beam-spot size and distribution do not contribute significantly to the final distribution.

V. MUON RUNS

The muon data permits an important test of the muon-identification efficiency, in that it checks the instrumental efficiency for detecting muons (and pions) and also tests our method of distinguishing μ's and π's. Table 1 gives the number of μ triggers and the number of particles detected in each of the chambers for a combined series of runs at 3 GeV/c, where A1 = 45 cm, A2 = 30 cm, and d = 79 cm (see Fig. 2a). The number of multiparticle events associated with the muon trigger is somewhat larger than we had expected but is consistent with δ-ray production in the iron[7] and in the chambers. Because of the large number of multiparticle events and the lack of spatial information for these events, we decided not to use multiplicity as a criterion for separating pions and muons in these tests. We therefore assume that multiparticle events have the same spatial distribution as the single-particle events and include them in the detected sample. Since we use the same procedure for the pion data, this tends to underestimate the true pion-rejection efficiency.

We may now check the efficiency of PC1, using the whole active area of the chamber as the detector. The efficiency of PC1 is easy to find since PC1 is large enough at its location in the iron to intercept all of the muons that produce a trigger. The efficiency is then

ε_{PC1} =

$$\frac{\text{\# of events detected by both planes + \# of multiparticle events}}{\text{\# of } \mu \text{ triggers}}$$

= 0.93 ± 0.02.

This can be compared with the earlier measurement over the center region of the chamber in which we found PC1 to be 97% efficient. PC2 does not intercept all of the μ triggers for the conditions of this run, and thus we cannot check its efficiency in this way. Instead, we assume that the efficiency of the whole chamber is the same as for PC1, since the efficiency measured at the center of the chamber is nearly the same, but we increase the estimated uncertainty obtaining ε_{PC2} = 0.93 ± 0.05.

We can also use the muon distributions at each of the locations PC1 and PC2 to check the multiple-Coulomb-scattering calculations. Figures 5b and 6b show the radial distributions of muons in PC1 for two runs where A1 = 30 cm and A1 = 45 cm, respectively. The smooth curves are the expected distributions using the Gaussian width determined from the multiple-Coulomb-scattering calculations and normalizing to the total number of events detected by PC1. The agreement with the data is quite reasonable.

VI. PION RUNS

A. One-Plane Muon Identifier

We can use the general procedures outlined above to calculate the pion rejection (or acceptance) of a one-plane muon identifier for various configurations of absorber thicknesses (A1 and A2) and drift spaces (d). The number of pions detected inside a circle large enough to contain 96% of the incident muons at PC1 or PC2 is first determined. The error in this number is assumed to be entirely statistical, and no error is assigned for the uncertainty associated with the radius of the circle. The number of pions is combined with the number of multiparticle events that would occur in the 96% circle, assuming that the multiparticle events have the same spatial distribution as the events recorded inside the chamber, and this sum is then corrected for the proportional-chamber inefficiency, $\varepsilon_{PC1} = 0.93 \pm 0.02$ or $\varepsilon_{PC2} = 0.93 \pm 0.05$.

An additional correction is made for proportional-chamber accidentals in the case of the pions, where often the pion associated with the trigger was either absorbed or scattered before reaching the chamber. This accidental rate was measured to be 2.8% for PC1 and 0.7% for PC2 by triggering on muons in the configuration A1 = 30 cm, A2 = 30 cm, and d = 94 cm with the scope display delayed by 3 μsec. This tests whether there is an accidental particle in the chamber long after the occurrence of the triggering muon. This type of accidental is not a problem when it occurs in coincidence with a real trigger

since it would then yield a multiparticle event and would be included in the sample anyway. Accidentals occurring after 75 nsec do not count at all because of the readout deadtime.

In order to use this correction for other absorber thicknesses, we must assume that the pion accidentals are attenuated along with the pions themselves, and this assumption is confirmed approximately by a comparison of the rates in PC1 and PC2. We assume also that the spatial distribution of the accidentals is similar to that of the pions. The accidental rate varies according to beam conditions, so we assign a relatively large accidental uncertainty of 1% in PC1 and 0.4% in PC2.

A correction is also made for the muons in the pion trigger. This correction is 0.2 to 0.4% of the pion triggers, depending on the geometry, and is unimportant except for extreme iron thicknesses. No correction is made for the protons (< 5%) in the pion trigger.

The pion acceptances for various cases are listed in Table 2. For a one-plane muon identifier, the acceptance does not depend strongly on the length of the drift space, since the size of the 96% muon circle increases with the length of the drift space. Therefore, the pion acceptance is plotted in Fig. 7 as a function only of the total absorber thickness for all of the cases listed in Table 2. We also show on the same graph one point taken with a negatively-charged beam and two points taken with a positive beam at 3.75 GeV/c. The line

drawn thru the points represents the average behavior of the data as a function of the iron thickness. The slope might be expected to decrease somewhat in magnitude at greater iron depths, since the size of the multiple-Coulomb-scattering envelope is increasing and more of the inelastically scattered pions might remain inside. The uncertainties in the data do not allow us to distinguish this type of behavior.

The average slope corresponds to an attenuation length of 16.6 cm and an effective "cross section" of 710 mb. This can be compared with an estimated pion-nuclear cross section for iron of 725 mb, obtained from π^+ data on copper at 3 GeV/c,[8] assuming that the inelastic cross section goes as $A^{2/3}$. We make the comparison with the inelastic cross section, since we expect this to be the dominant process in separating pions and muons.[9]

The radial distributions of the pions remaining after 30 cm and after 45 cm of iron are shown in Figs. 5a and 6a, respectively. The smooth curve thru the data is the expected distribution for multiple Coulomb scattering. The pion data of Fig. 6a can be approximated with a Gaussian distribution of slightly increased width, $\sigma \approx 4$ cm rather than 3 cm, which is explained if we combine the expected contribution for nuclear elastic scattering ($\theta \approx 20$ mrad) in quadrature with the contribution due to multiple Coulomb scattering. The pion data of Fig. 5a shows even less broadening, demonstrating a larger population of non-interacting pions. The remaining

pions are then predominantly those that have not interacted strongly or that have elastically scattered, and such pions are not distinguishable from muons in the one-plane muon identifier.

Figure 8 shows what happens to the pion acceptance and the calculated muon acceptance when the area of the acceptance circle is changed. These data are obtained from the raw distributions in PC1 (no corrections) with A1 = 45 cm and d = 79 cm for a 3-GeV/c pion beam. The absolute values are shifted slightly since we have ignored normalization corrections, but the general behavior of the data should be correct. The errors shown are statistical only.

B. Two-Plane Muon Identifier

The 35-mm pictures showing one event per frame allow us to determine the improvement in the pion rejection efficiency that results from a muon identifier in which two detector planes are used. One advantage of the two-chamber configuration is that the first chamber allows the direction of the particle to be redefined, and this leads to a smaller multiple Coulomb scattering envelope at the location of the second chamber. Some pions that would be included in the 96% circle of a one-plane muon identifier will now be outside the smaller, redefined 96% circle of a two-plane identifier at the second plane.

The 35-mm pictures are taken under the conditions

A1 = 30 cm, A2 = 30 cm, and d = 94 cm. In this configuration, PC2 is geometrically smaller than the size of the 96% circle at this location, so that none of the pion triggers detected in PC2 can be identified as pions under the analysis of a one-plane muon identifier. In order to determine the direction of the particle at PC1, we assume that the scattering takes place along the beam line at the center of absorber A1. The angle of the particle relative to the beam direction is then given by $\tan\theta \approx r/109$, where r is the displacement from the beam axis in cm at PC1. From the direction and location of the particle in PC1, we can predict the particle's unscattered position at PC2. The difference between the actual position and the predicted position is then determined. For muons, the distribution of this difference depends on the multiple Coulomb scattering in absorber A2 and the uncertainty in the redefinition of the particle direction. The rms radius at PC2 due to A2 only is 1.3 cm, while the radius is 6 cm if we must include the contribution from absorber A1 (no redefinition).

The distribution of events as a function of the difference between the observed and predicted locations at PC2 is shown in Fig. 9 for both muon and pion triggers. The muon triggers yield a distribution which is narrower than the pion distribution. For example, if we consider only muons with a difference less than 5 cm, then we lose 5% of the muon triggers while identifying 17% of the remaining pions. The estimated

radius of the redefined 96% circle at PC2 is 3.2 cm including the contributions of the non-zero width of the beam and multiple Coulomb scattering in A2, but neglecting the effects of uncertainties in the particle direction redefinition. This is not a tremendous increase in the pion rejection efficiency, which again demonstrates that the remaining pions are predominantly those that have not interacted or that have scattered elastically yielding a small scattering angle.

The main advantage of a two-plane identifier would therefore be to add redundancy that might be beneficial in sorting out many-particle hits in a large array of multi-wire proportional chambers.

VII. CONCLUSION

We have investigated experimentally a technique for distinguishing high-energy muons from hadrons in which the hadrons signal their identity by interacting strongly within a relatively thin absorber. By taking into account multiple Coulomb scattering in the absorber, as well as the uncertainties in the incident trajectory, a region can be defined in the detector plane in which the incident particle, if it is a muon, is likely to be found. The reaction products from incident hadrons will normally be outside of the muon-acceptance region, even though the associated radiation may be capable of penetrating to a much greater depth in the absorber. A detector plane consisting of multi-wire proportional chambers will provide the spatial resolution required by this technique and offers a number of other important advantages.

A very specific implication of these tests is that it should be possible to distinguish muons from hadrons emerging from the NAL 15-foot bubble chamber simply by installing a single plane of multi-wire proportional chambers immediately behind the bubble chamber. The magnet coils surrounding the bubble chamber, plus an equivalent absorber between these coils, can serve as the interaction material for hadrons. In this simple configuration, equivalent to about 50 cm of iron, it should be possible to reject 96 ± 1% of the pions while retaining 96% of the muons incident in the region covered by the muon identifier.

We appreciate the help of James Marriner and Art Ogawa in the setting up and running of this experiment. We are deeply grateful to Dr. Herbert Steiner for the use of the individual channel read out electronics and for his suggestions, which made their use successful. We also appreciate the support of the Bevatron staff that made this run possible.

REFERENCES

1. See, for example, the following National Accelerator Laboratory Summer Studies: D.D. Jovanovic, R. Palmer, and B. Roe, "Muon Detectors After the 25-Foot Chamber," NAL 1969 Summer Study Report SS-69, Vol. II, p. 207; L. Clavelli and R. Engelman, "Theoretical Questions and Measurements of Neutrino Reactions in Bubble Chambers," NAL 1970 Summer Study Report SS-199, p. 255; R. Palmer, "Muon Detection with a Plate Inside the 15-Foot NAL Bubble Chamber," NAL 1970 Summer Study Report SS-201, p. 279; A. Mukhin and D. Yount, "External Versus Internal Muon Identification in the 15-Foot Bubble Chamber," NAL 1970 Summer Study Report SS-186, p. 295. NAL Proposals #9, #28, #44, #53, and #92 are among those that explicitly discuss muon identification.

2. A. Boyarski, SLAC-PUB-559 (1969); and S. Eklund (private communication). We are particularly grateful to these authors and their colleagues at SLAC for providing us with typical raw-data samples taken with the 20-GeV spectrometer system. The curves shown in Fig. 1 are based on our own analysis and interpretation of these raw data samples.

3. Particle Data Group, Rev. Mod. Phys. 43, 51 (1971).

4. S. Parker, R. Jones, J. Kadyk, M.L. Stevenson, T. Katsura, V.Z. Peterson and D. Yount, Nucl. Instr. and Methods 97, 181 (1971).

5. L. Eyges, Phys. Rev. 74, 1534 (1948); R.M. Sternheimer, Review of Scientific Instruments 25, 1070 (1954).

6. B. Rossi, High Energy Particles (Prentice-Hall, Inc., Englewood Cliffs, N. J., 1961), p. 72.

7. W. Hazen, Phys. Rev. 64, 7 (1943); W.W. Brown, Phys. Rev. 76, 506 (1949).

8. M.J. Longo and B.J. Moyer, Phys. Rev. 125, 701 (1961).

9. A.D. Johnson, M.W. Peters, and V.J. Stenger, "Performance of an External Muon Identifier," HEPG Report NO. UH-511-97-71, April 1971. (unpublished).

TABLE CAPTIONS

Table 1 Number of muons detected in PC1 and PC2 for a 3 GeV/c run with A1 = 45 cm, A2 = 30 cm, d = 79 cm, and for 381 muons incident.

Table 2 Fraction of pions remaining in 96% muon circle for various run conditions.

TABLE 1

Number of muon triggers	381
Number detected by chamber 1 (both x and y)	337
Number of multiparticle events in chamber 1	18
Number detected plus number of multiparticle events	355
Number detected by chamber 2 (both x and y)	269
Number of multiparticle events in chamber 2	62
Number detected plus number of multiparticle events	331

TABLE 2

Run	A1 (cm Fe)	A2 (cm Fe)	d (cm)	Chamber used as detector	Total (cm) detector absorber	Incident momentum (GeV/c)	Percent π's remaining
1	5	0	19	PC2	5	+ 3	67 ± 12
2	10	0	19	PC2	10	+ 3	57 ± 9
3	15	0	19	PC2	15	+ 3	42 ± 11
4	30	30	94	PC1	30	- 3	13.8 ± 0.9
5	45	30	19	PC1	45	+ 3	6.1 ± 0.7
6	45	30	69	PC1	45	+ 3	5.7 ± 0.6
7	45	30	79	PC1	45	+ 3	5.9 ± 0.8
8	30	30	19	PC2	60	+ 3	3.1 ± 0.8
9	45	30	19	PC2	75	+ 3	1 ± 1
10	45	30	79	PC1	45	+ 3.75	6 ± 1
11	45	30	79	PC2	75	+ 3.75	2 ± 1

FIGURE CAPTIONS

Fig. 1 Pion range data from the SLAC 20-GeV spectrometer. The ordinate gives the fraction of the incident pions that generate penetrating radiation versus the absorber thickness in equivalent cm of iron. Because the reaction secondaries tend to penetrate deeper as the incident momentum increases, the curves shift to the right with increasing momentum. Ultimately, however, the slopes become similar for different incident momenta, a consequence of the fact that the original pion-nuclear reaction cross section is relatively constant over this momentum range.

Fig. 2 a. Experimental apparatus. The muon identifier is simulated by two iron absorbers, A1 and A2, of variable thickness; a variable drift space d; and x-y proportional chambers, PC1 and PC2. Other elements in the beam line, including a gas Cerenkov counter upstream (not shown) are used to distinguish protons, pions, and muons.

b. Root-mean-square radius, R_{rms}, for multiple Coulomb scattering of muons traversing the configuration shown in Fig. 2a.

Fig. 3 Attenuation curves for a beam of positively-charged particles of 3 GeV/c as a function of the total amount of iron in front of S5. The upper curve is for protons, pions, and muons, while the lower curve, with the

Cerenkov counter in coincidence, results primarily from pions and muons.

Fig. 4 a. Display of x-y event distributions obtained from multiwire proportional chambers PC1 and PC2 for 1453 incident π^- at 3 GeV/c.

b. Display of x-y distributions from PC1 and PC2 with no absorber preceding chambers.

Fig. 5 Radial distributions for pions (a) and muons (b) in PC1 for Al = 30 cm and d = 94 cm. The smooth curves are calculated for multiple Coulomb scattering using a Gaussian formula normalized to give the total number of events detected by PC1. The agreement with the muon curve is excellent, while the data for surviving (non-strongly-interacting) pions are somewhat broader.

Fig. 6 Radial distributions for pions (a) and muons (b) in PC1 for Al = 45 cm and d = 79 cm. As in Fig. 5, the smooth curves are calculated for multiple Coulomb scattering.

Fig. 7 Fraction of the incident pions surviving within a multiple-Coulomb-scattering circle containing 96% of the incident muons, plotted as a function of the thickness of iron in cm.

Fig. 8 Plot versus detector area of the muon-acceptance efficiency (left-hand scale) and pion-acceptance efficiency (right-hand scale). The pion data were obtained at 3 GeV/c from the raw distribution in PC1

(no corrections applied) with A1 = 45 cm and d = 79 cm.

Fig. 9 Number of events as a function of the difference between the predicted particle position and the actual position at PC2 for pions (a) and muons (b). The data were obtained at 3 GeV/c with A1 = 30 cm, A2 = 30 cm, and d = 94 cm. The predicted position is obtained by redefining the particle direction at PC1. All of the events are inside the 96% circle at PC2 under the analysis of a one-plane muon identifier.

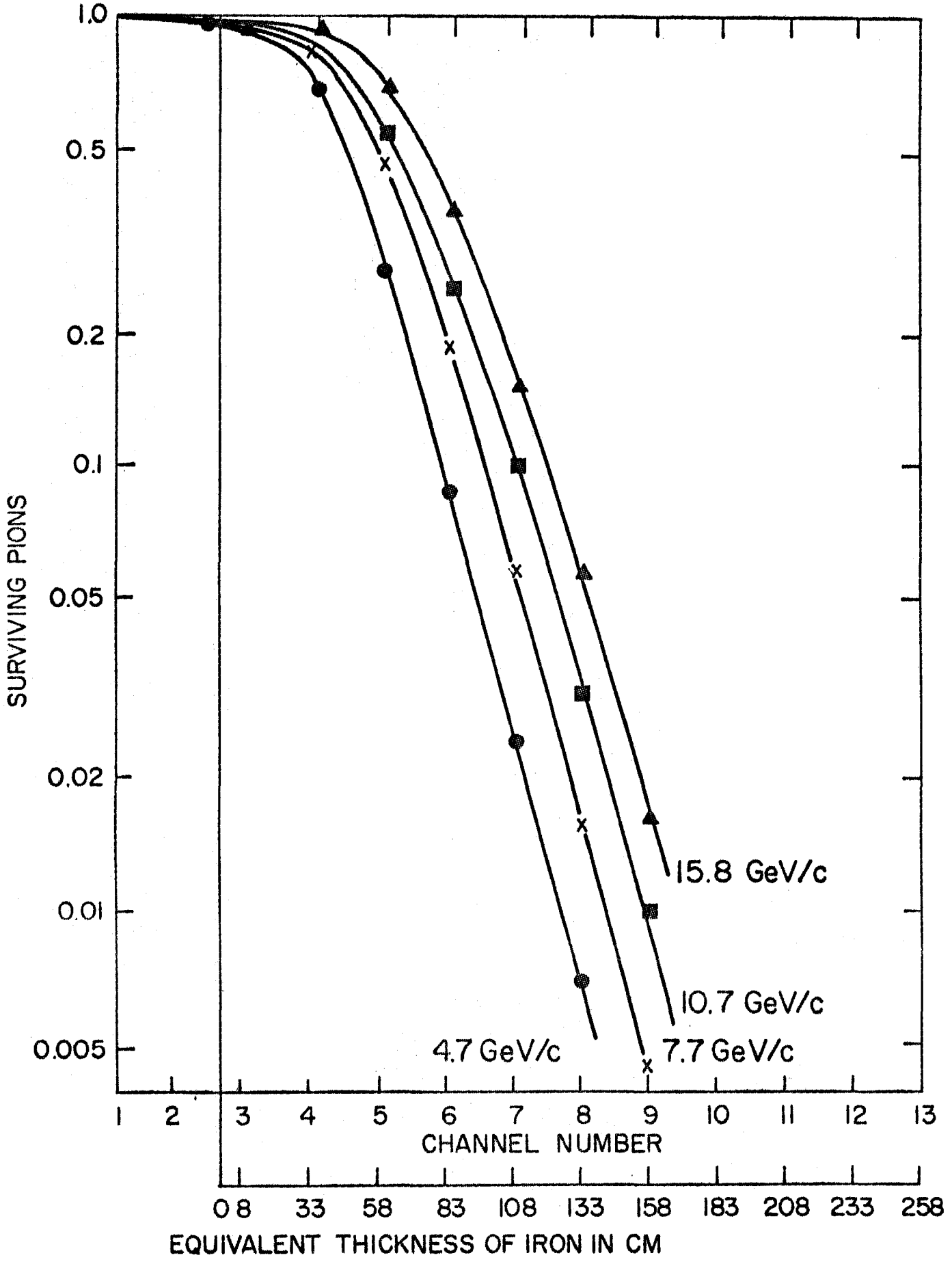
1.0
0.5
0.2
0.1
0.05
0.02
0.01
0.005
SURVIVING PIONS
15.8 GeV/c
10.7 GeV/c
7.7 GeV/c
4.7 GeV/c
1 2 3 4 5 6 7 8 9 10 11 12 13
CHANNEL NUMBER
0 8 33 58 83 108 133 158 183 208 233 258
EQUIVALENT THICKNESS OF IRON IN CM

FIG. 1

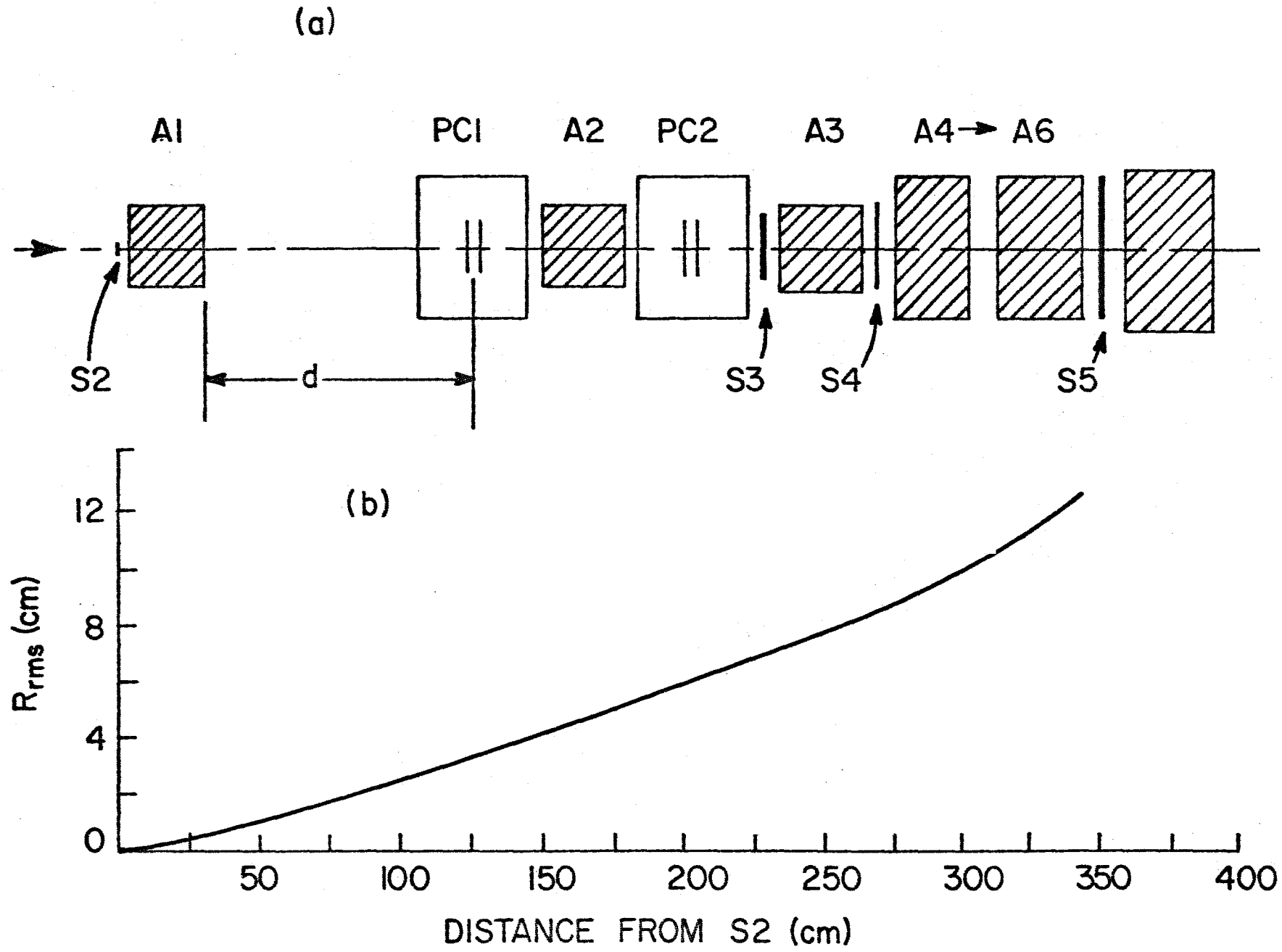

FIG. 2

TM-358
2610.900

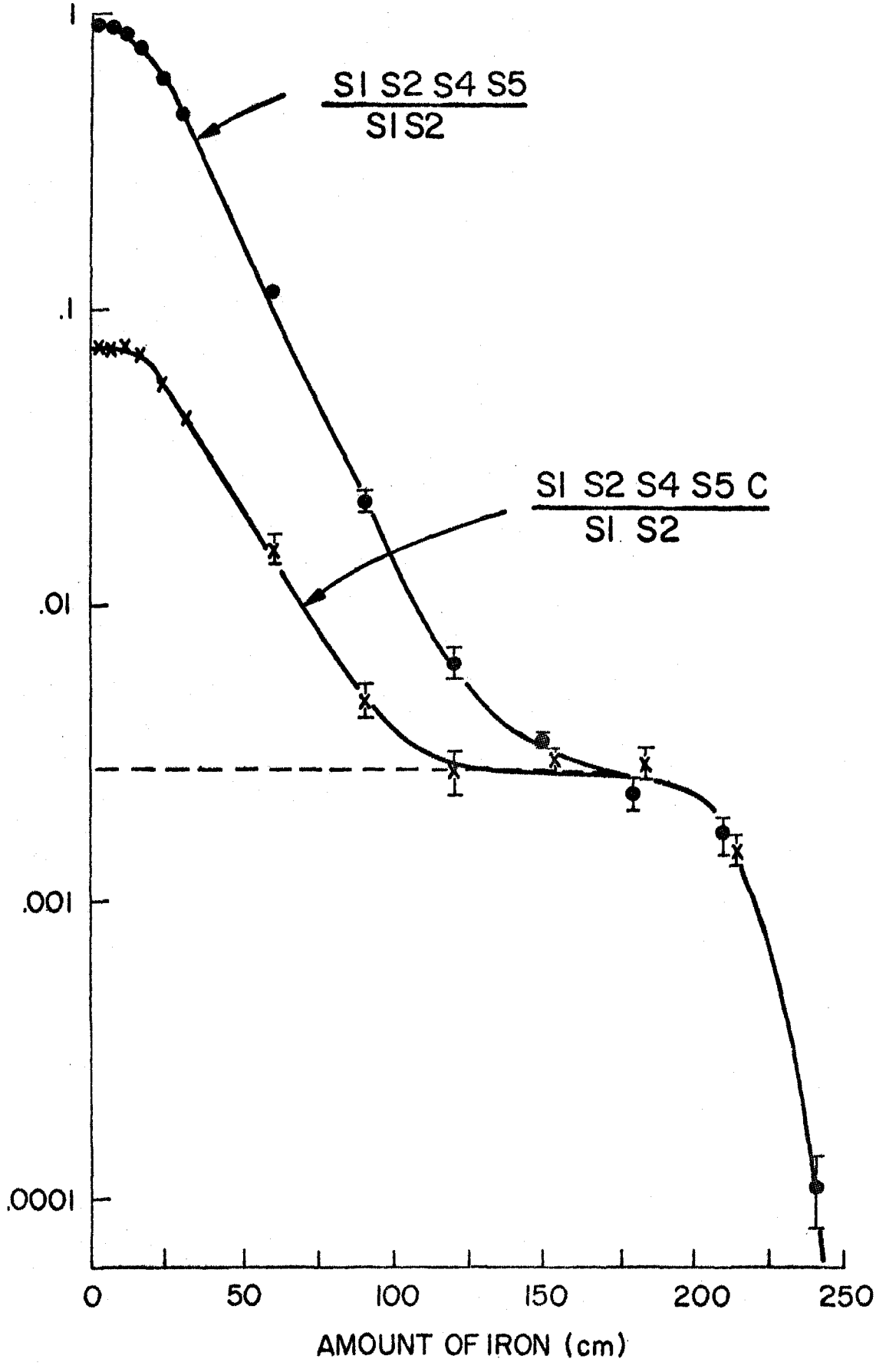
1
.1
.01
.001
.0001
S1 S2 S4 S5
S1 S2
S1 S2 S4 S5 C
S1 S2
0
50
100
150
200
250
AMOUNT OF IRON (cm)

FIG. 3

(a)

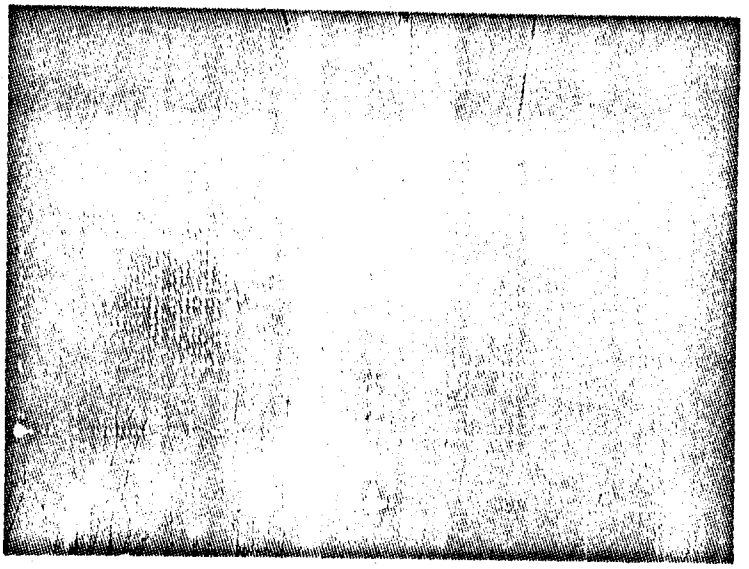

Pc1 Pc2

(b)

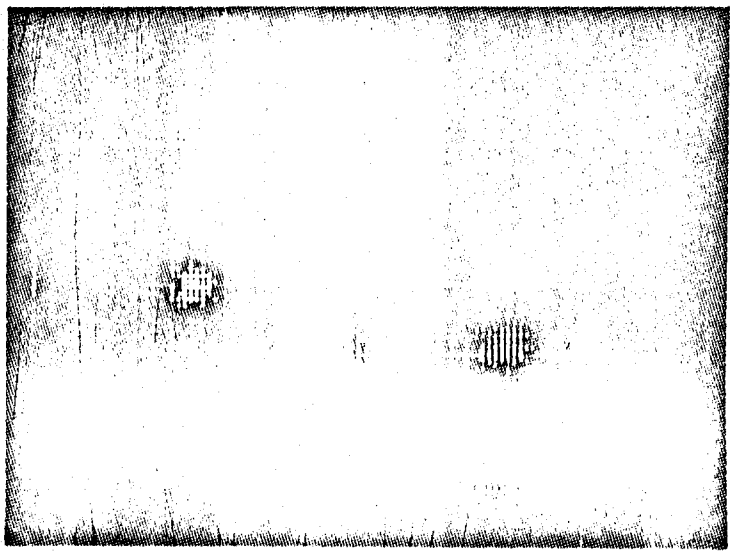

Pc1 Pc2

FIG. 4

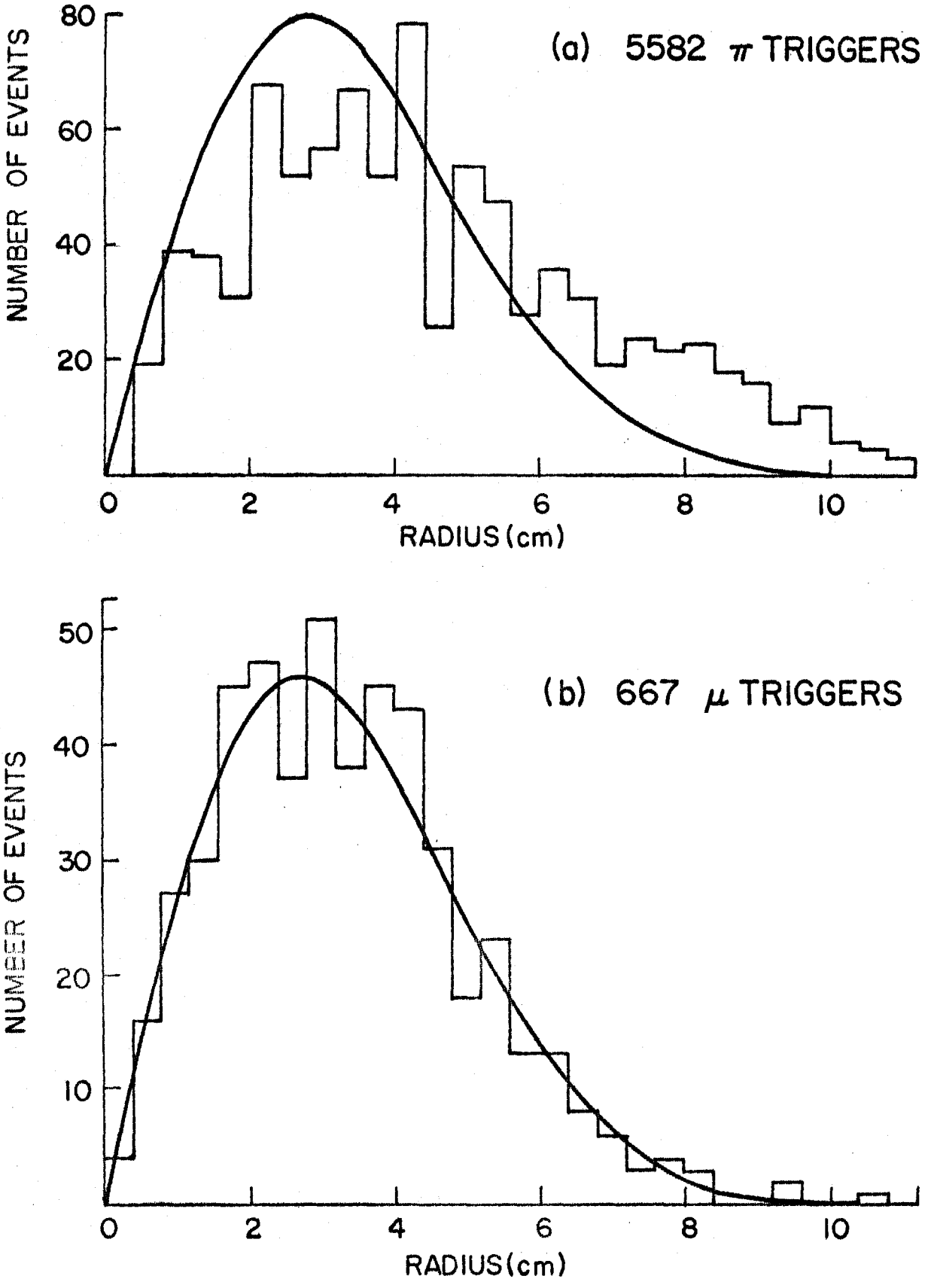
(a) 5582 π TRIGGERS
NUMBER OF EVENTS
80
60
40
20
0
2
4
6
8
10
RADIUS (cm)
(b) 667 μ TRIGGERS
NUMBER OF EVENTS
50
40
30
20
10
0
2
4
6
8
10
RADIUS (cm)

FIG. 5

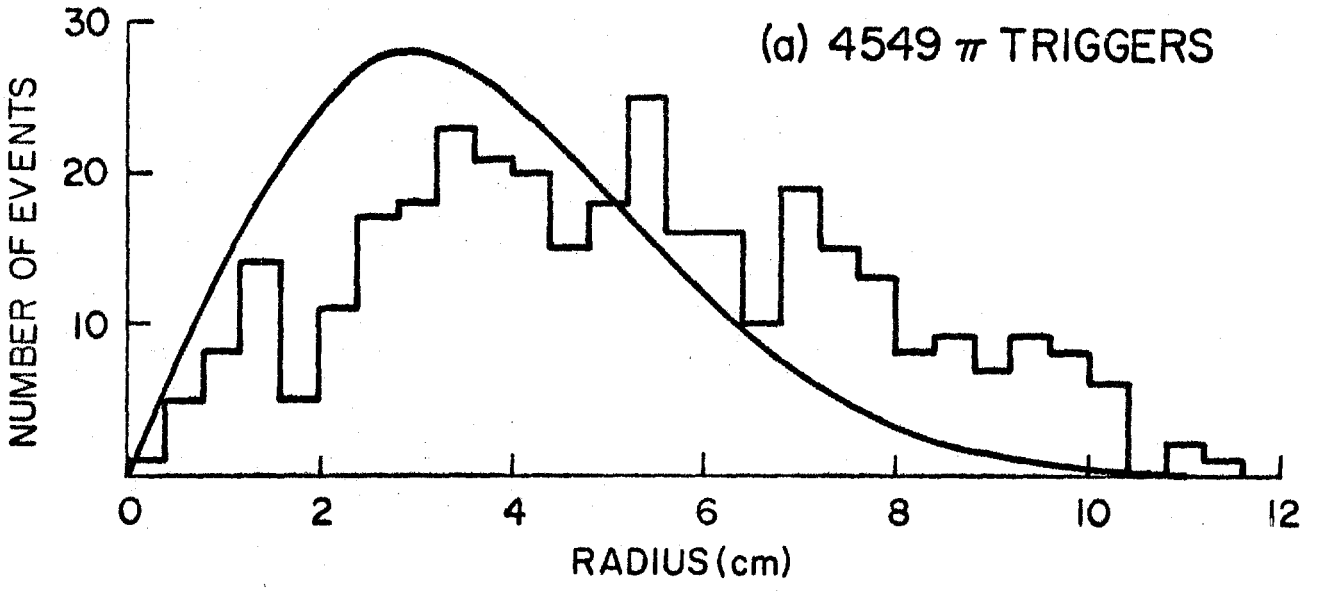
(a) 4549 π TRIGGERS
NUMBER OF EVENTS
30
20
10
0
2
4
6
8
10
12
RADIUS (cm)

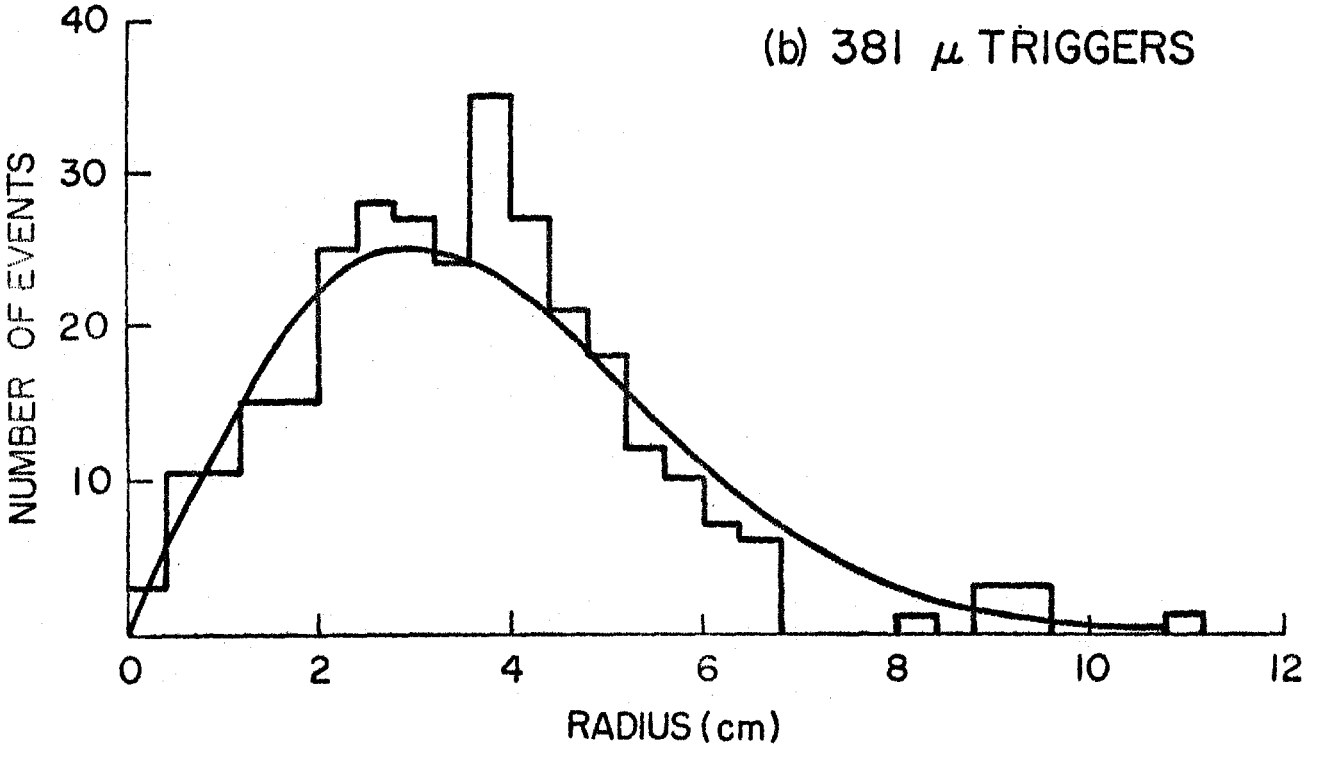
(b) 381 μ TRIGGERS
NUMBER OF EVENTS
40
30
20
10
0
2
4
6
8
10
12
RADIUS (cm)

FIG. 6

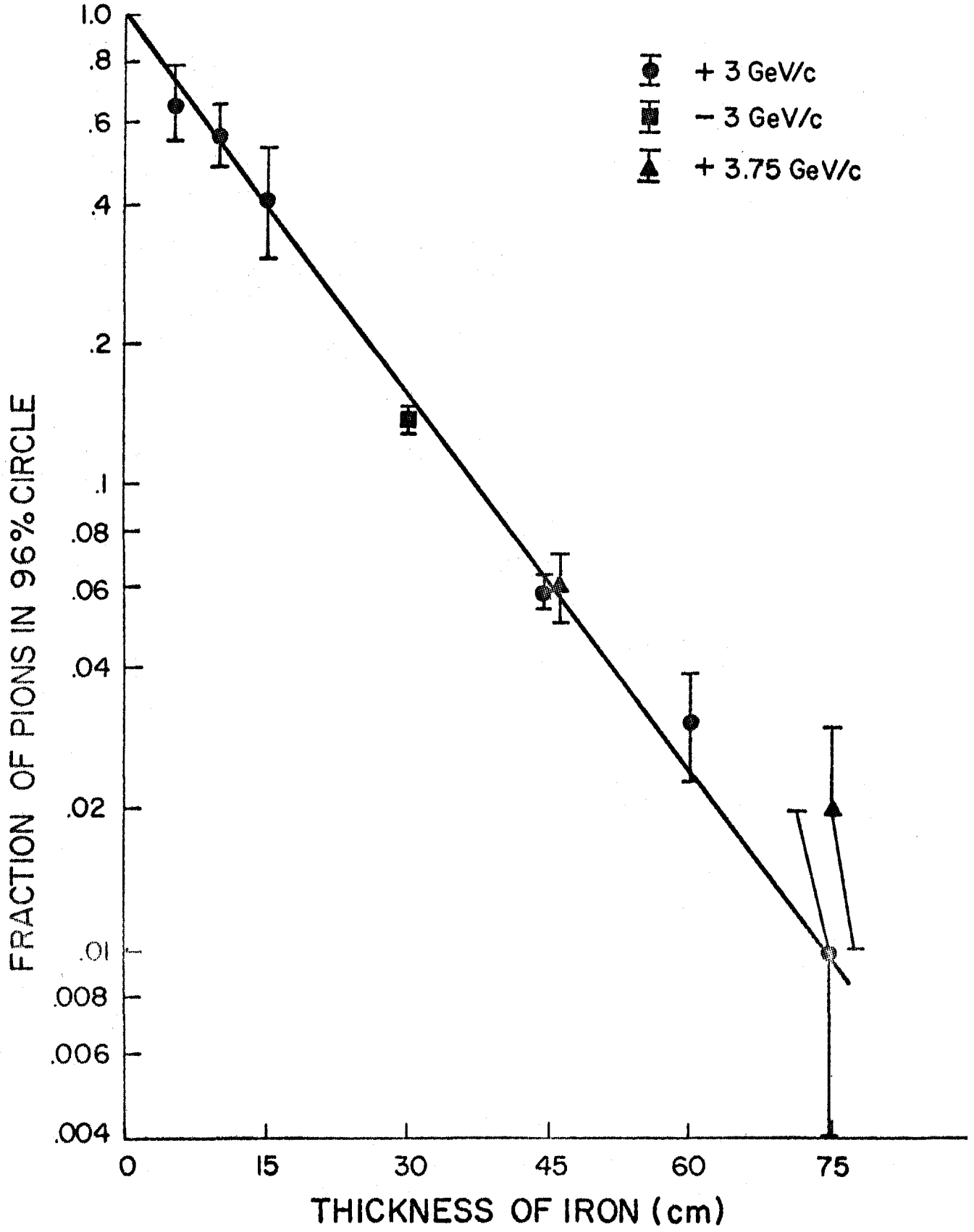
+ 3 GeV/c
− 3 GeV/c
+ 3.75 GeV/c
FRACTION OF PIONS IN 96% CIRCLE
1.0
.8
.6
.4
.2
.1
.08
.06
.04
.02
.01
.008
.006
.004
0
15
30
45
60
75
THICKNESS OF IRON (cm)

FIG. 7

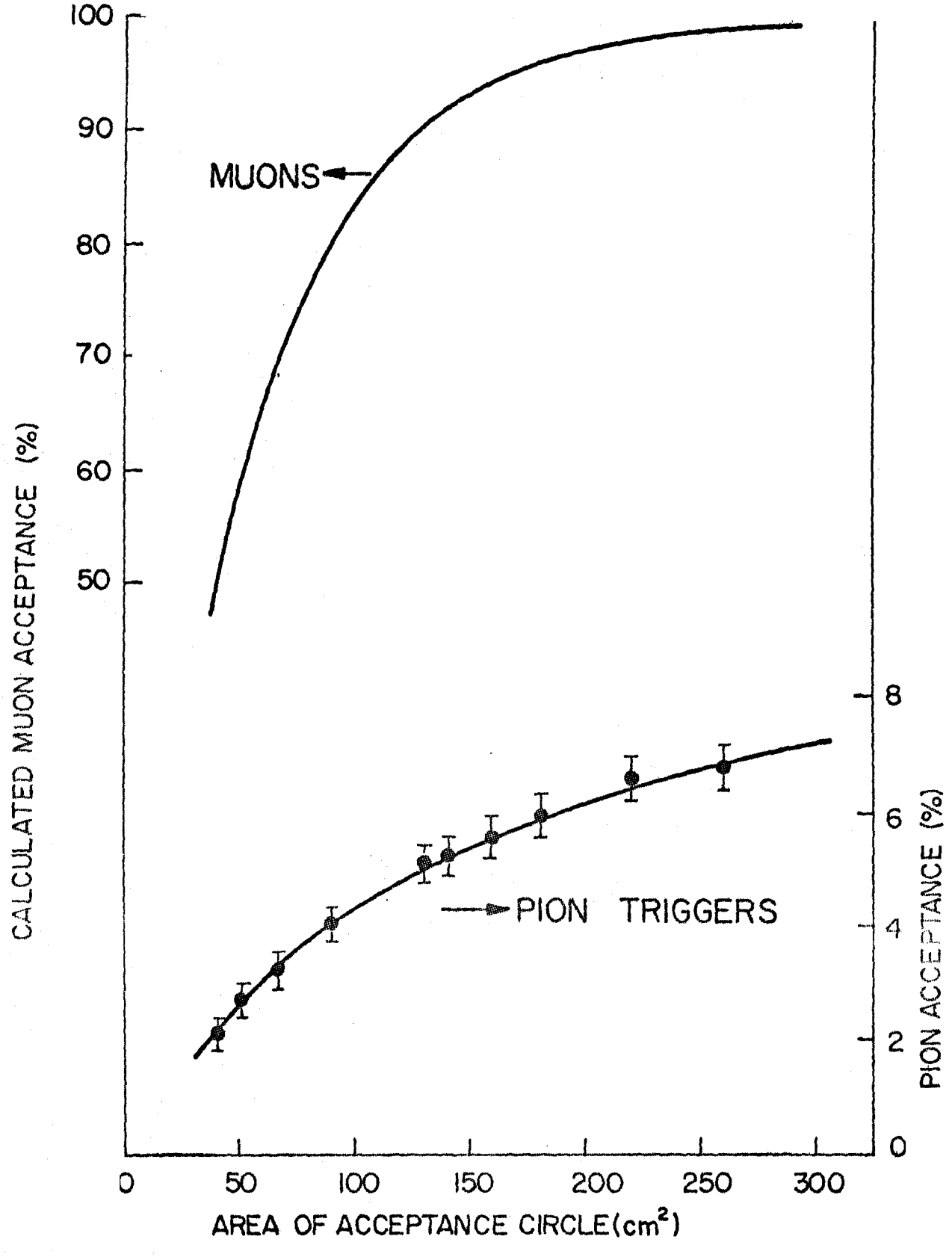
100
90
80
70
60
50
MUONS
CALCULATED MUON ACCEPTANCE (%)
8
6
4
2
0
PION ACCEPTANCE (%)
PION TRIGGERS
0
50
100
150
200
250
300
AREA OF ACCEPTANCE CIRCLE(cm²)

FIG. 8

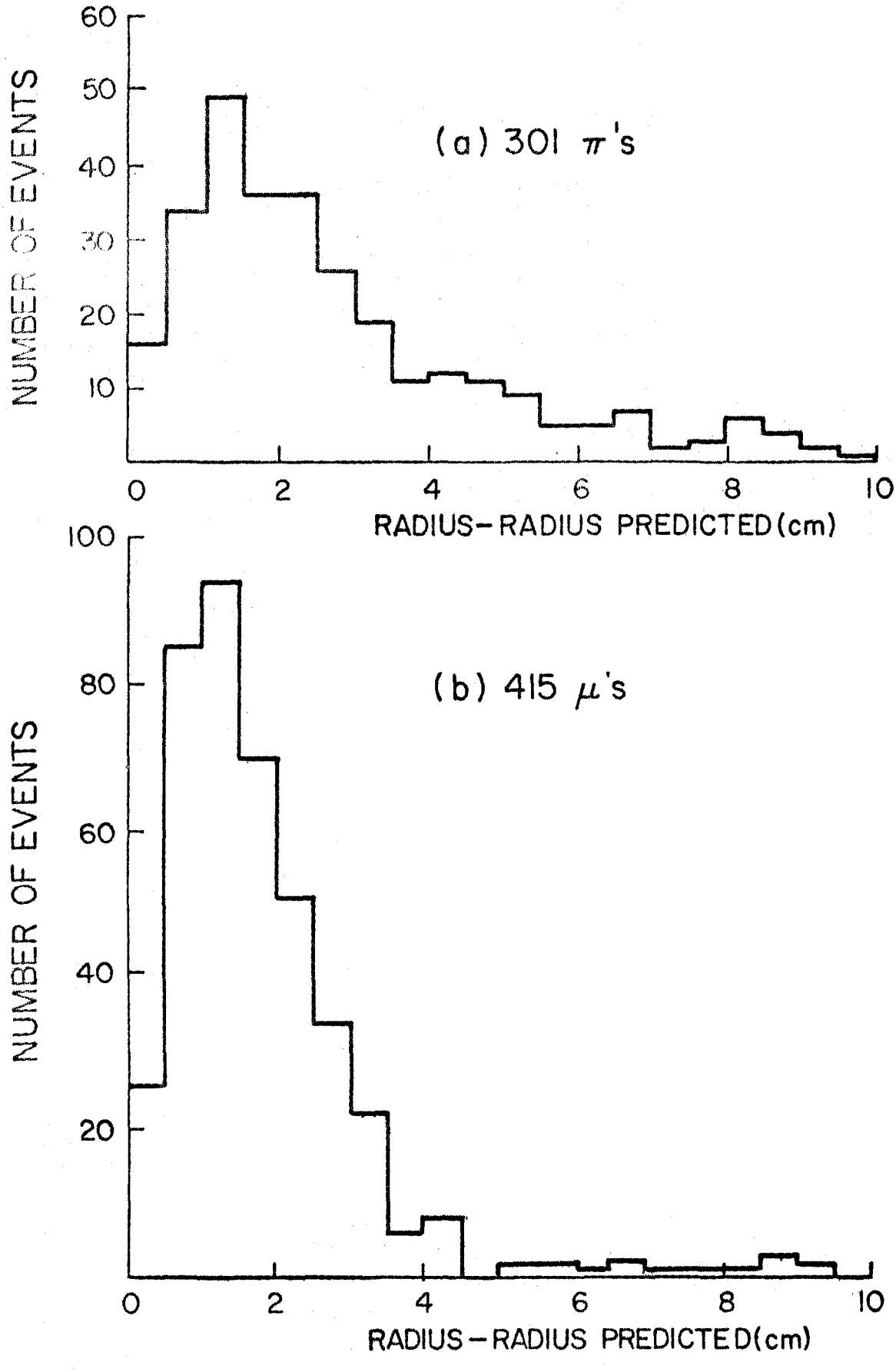
(a) 301 π's
NUMBER OF EVENTS
RADIUS – RADIUS PREDICTED (cm)
(b) 415 μ's
NUMBER OF EVENTS
RADIUS – RADIUS PREDICTED (cm)

FIG. 9